Local structural and chemical ordering of nanosized $Pt_{3\pm\delta}Co$ probed by multiple-scattering x-ray absorption spectroscopy

Giorgia Greco,[1,*] Agnieszka Witkowska,[2,†] Emiliano Principi,[1]
Marco Minicucci,[1] and Andrea Di Cicco[1,3]

[1]*CNISM, School of Science and Technology, Physics Division, University of Camerino, I-62032 Camerino (MC), Italy*
[2]*Department of Solid State Physics, Gdansk University of Technology, PL-80-233 Gdansk, Poland*
[3]*IMPMC-CNRS, Université P.et M. Curie, 140 rue de Lourmel, F-75015 Paris, France*

(Received 30 November 2010; revised manuscript received 3 February 2011; published 5 April 2011)

This work reports a detailed investigation of the local structure and chemical disorder of a $Pt_{3\pm\delta}Co$ thin film and $Pt_{3\pm\delta}Co$ nanoparticles. We have used a combination of techniques including x-ray absorption spectroscopy (XAS), x-ray diffraction (XRD), and high-resolution transmission electron microscopy (TEM). High-quality XAS spectra at the Co K edge and Pt L_3 edge have been analyzed using double-edge multiple-scattering data analysis. Structural extended x-ray absorption fine structure (EXAFS) refinements have been performed accounting for the reduction of the coordination numbers and degeneracy of three-atom configurations, resulting from the measured size distribution and stoichiometry. The important effect of chemical ordering on pair and three-atom configurations has been studied using computer simulations based on a simple model accounting for substitutional disorder, defined by an order parameter s. It has been found that individual EXAFS signals related to the minority species (Co) are extremely sensitive to substitutional disorder so their intensities, especially those of the collinear three-atom configurations, can be used as a measure of the ordering level. The thin film has been found to be chemically disordered ($s \leqslant 0.4$), in agreement with previous estimates. The $Pt_{3\pm\delta}Co$ nanoalloy has been found to be partially ordered ($s = 0.6 \pm 0.1$) while the local structure around Co atoms is characterized by a higher level of structural disorder as compared to the bulk-like thin film. The robust approach for nanomaterial characterization used in this work combining different techniques can, in principle, be applied for structural refinements of any binary nanocrystalline functional system.

DOI: 10.1103/PhysRevB.83.134103 PACS number(s): 61.46.−w, 61.05.cj, 36.40.Mr, 82.45.Yz

I. INTRODUCTION

Understanding the structure and dynamics of nanomaterials as well as their physicochemical properties is currently regarded as a challenging research activity having crucial consequences in materials design for various novel applications. In this work, we focus our attention on the structural characterization of simple bimetallic nanomaterial, as opposed to their bulk analog, using advanced x-ray absorption spectroscopy (XAS) data analysis.[1–4]

Metal nanoparticles of close-packing metals attract huge interest in applications, and they are now commonly used in our daily life. For example, supported metal nanoparticles of noble metals like Pt, due to their catalytic activity, are used in various applications, including fuel-cell technology. Binary Pt-based alloys with various transition metals, such as V, Cr, Co, Ti, and Ni, as well as ternary alloys, that exhibit higher oxygen reduction reaction (ORR) electrocatalytic activities than Pt alone[5–7] are commonly used as a cathode catalyst in proton-exchange membrane fuel cells (PEMFCs). Among them, the platinum cobalt nanoalloy catalyst seems to be very promising.[7] Previous experimental works[8–12] on these kinds of nanocatalysts show that the increase in the kinetics of ORR compared to pure Pt could be attributed to changes in the geometric structure (i.e., Pt-Pt bond distance, number of Pt nearest neighbors, surface composition), in the electronic structure (i.e., orbital energy levels, strength of interaction between atoms) and to the nature and coverage of surface oxide layers. But the matter is still debated and very few works are devoted to fine analysis of nanostructures and possible correlations between structure and morphology and functional properties.

This work is devoted to the structural characterization of a standard bimetallic Pt-Co nanomaterial, using a combination of advanced techniques like XAS, high-resolution transmission electron microscopy (HRTEM), and x-ray diffraction (XRD). Establishing new protocols for characterization of functional binary nanoalloys is an important step in our knowledge per-se, and it is an important starting point to understand the slight structural local changes appearing during these nanomaterials operation. The detailed structural refinement of the Pt-Co catalyst presented in this work has been performed using advanced multiple-scattering (MS) XAS data analysis, assisted by the combination of the above-mentioned techniques. As is well known, the XAS technique is sensitive to the local structure up to 5–10 Å around photoabsorbing sites, selected by their atomic number, and, for this reason, it is a very useful tool for the study of nanostructural materials.[1–4,13] We have performed here a multiple scattering (MS) double-edge (Co K and Pt L_3) analysis of extended x-ray absorption fine structure (EXAFS) signals by using the GNXAS method[14,15] (the acronym is formed by the combination of GN, indicating the n-body distribution functions, g_n, and XAS).

The aim of this work is, on the one hand, to establish a reliable methodology for fine structure analysis of nanosized chemically disordered systems and, on the other hand, to obtain a full structural characterization of a binary alloy of particular interest in applications. To this aim, we have developed a simple model accounting for chemical disorder, which is

known to be present in this class of systems, applied both to a bulk-like thin film alloy, taken as reference for the structure, and to the nanosized system.

The paper is organized as follows: Section II is dedicated to sample characterization by using TEM and XRD techniques (i.e., detailed analysis of nanocrystalline morphology and size distribution). Section III is focused on the methodology of the XAS data analysis using an advanced technique based on the GNXAS method[14,15] in application to binary alloys. Results of the MS XAS data analysis of $Pt_{3\pm\delta}Co$ thin film and samples with $Pt_{3\pm\delta}Co$ nanoparticles are shown and discussed in Sec. IV. In Sec. V the main conclusions of this work are given.

II. NANOCRYSTALLINE SAMPLE CHARACTERIZATION

The accurate XAS experiments discussed in this work have been performed on a nanocrystalline Pt-Co alloy supported on Vulcan (E-TEK^{TM} product composed of 30% PtCo(1 : 1) and 70% of black carbon Vulcan XT-72).

The average size of the considered platinum cobalt nanocrystallites is around 3–5 nm according to the data sheet of the producers and as reported in Ref. 17 in an independent study. However, proper detailed sample characterization including stoichiometry, size distribution, and lattice structure is needed to perform a careful and reliable XAS data analysis in this ill-ordered nanosized system. In fact, it is known that platinum cobalt alloys can crystallize in both face-centered cubic (fcc) and tetragonal phases (depending on the alloy composition), in ordered and substitutionally disordered form.[16] Moreover, single-phase nanoalloy crystals are rather difficult to obtain. Therefore, detailed morphological investigation should be performed prior to any XAS analysis in order to study crystallite size distribution and their shape and homogenous distribution through the sample (see also Refs. 12,13,18,19). We have used transmission electron microscopy (TEM; JOEL JEM-2100F) and x-ray diffraction (XRD; for setup description see Ref. 20) measurements to obtain essential mesoscopic and nanoscopic information about the samples.

TEM-image analysis (500 randomly selected quasispherically shaped particles) of samples was carried out to study the actual nanoparticle size distributions. Figures 1(a) and 1(b) show typical TEM and HRTEM images of platinum cobalt nanoparticles, and Fig. 1(c) presents their size distribution. It should be noted that the distribution is asymmetric and shows a tail extending to large-sized nanoparticles. The size distribution can be reproduced rather accurately through a log-normal model.[21,22] The size distribution maximum and mean values (d_{max} and d_{mean}, respectively) and the distribution broadening (σ) are shown in Table I. HRTEM images of

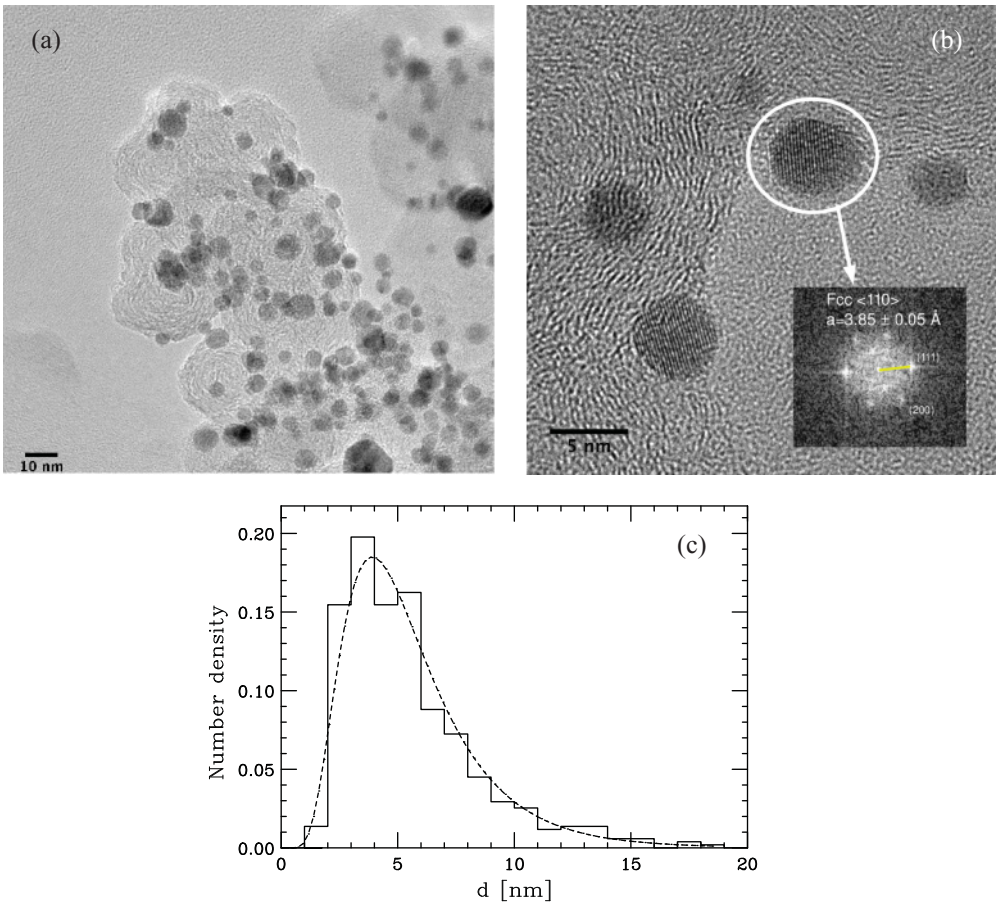

FIG. 1. (Color online) Top-left: TEM and top-right: HRTEM images of platinum cobalt nanoparticles supported on Vulcan (E-TEK^{TM}). In the inset, fast Fourier transform (FFT) of the HRTEM image of nanoparticle shows lattice reflections. Bottom: Metallic nanoparticle size distribution obtained by TEM images analysis.

TABLE I. The results of the platinum cobalt nanocrystalline sample characterization. The first row shows the results of the XRD peak-profile analysis: mean diameter d_{mean} of platinum-cobalt nanocrystals and the lattice parameter a. The second row shows the TEM images analysis results: the size distribution maximum and the mean value, d_{max} and d_{mean}, respectively, the distribution broadening σ, and the lattice parameter a obtained from HRTEM-images FFT analysis of 10 particles. f_{Co} is the Co atomic fraction obtained by Vegard's law [see Eq. (1)]. The third row shows the Pt : Co stoichiometry and f_{Co} obtained by the ratio of the XAS discontinuity at the Pt L_3 and Co K edges.

Pt-Co/C Nanoalloy	d_a [Å]	d_{max} [nm]	d_{mean} [nm]	σ [nm]	f_{Co}	Pt : Co
XRD	3.844(5)		4.3(9)		0.24(1)	3.16(3) : 1
TEM	3.80(5)	3.5(5)	5.5(5)	2.68(8)	0.3(1)	2.3(8) : 1
XAS					0.27(1)	2.65(4) : 1

nanoparticles have also been used to determine their crystal structure by performing fast-Fourier-transform (FFT) analysis. One example of an obtained FFT image is shown as an inset in Fig. 1(b), whereas resulted from their analysis fcc lattice constant is presented in Table I.

The mean size and crystal structure of the platinum cobalt crystallites have also been estimated by analyzing the x-ray diffraction pattern. We considered the shape of the (111), (200), (220), (311), and (222) peaks, as shown in Fig. 2. Peak profiles have been modelled with a Voigt function, using a Gaussian component to correct for instrument contribution to peak broadening ($\sigma_{corr} = 0.1^\circ$) (program PEAKFIT; see, e.g., Refs. 25,26). The nanoparticle size has been estimated through the Scherrer equation,[23,24] using 1.0 (not completely uniform distribution) as the Scherrer constant. The result is presented in Table I. The peaks positions show that the bimetallic catalyst

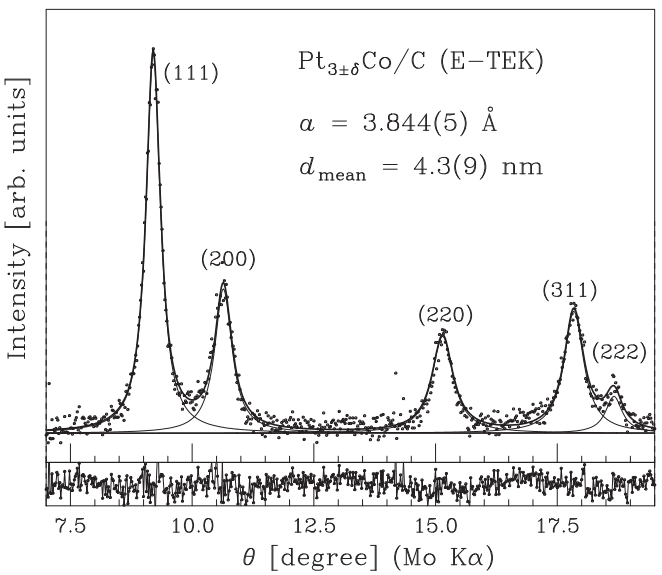

FIG. 2. X-ray powder diffraction pattern of the platinum cobalt nanoparticles supported on Vulcan (E-TEK™). Experimental data (points) are compared with the calculated pattern modelled using Voigt functions (solid lines). The residual curve is shown below the diffraction pattern.

is characterized by a crystalline fcc structure. No additional peaks or shoulders are observed, which indicates that the nanoparticles consist of this single crystalline phase.

The Co atomic fraction f_{Co} in the considered nanoalloy can be evaluated by Vegard's law: [27–29]

$$f_{Co} = \frac{a - a_o}{a_s - a_o} f_s, \quad (1)$$

where a_o and a_s are the lattice parameters of pure Pt (0.3925 nm) and PtCo alloy (0.375 nm[30]), respectively. The fraction f_s is the reference Co alloy atomic fraction in PtCo ($f_s = 0.5$).[27,31]

In Table I we report the f_{Co} values and Pt : Co stoichiometries obtained by using the above-mentioned Vegard's law and XRD- and TEM-extracted lattice parameters and by the ratio (weighted according to the tabulated x-ray cross sections) of the XAS discontinuity at the Pt L_3 and Co K edges. Present results indicate that the average stoichiometry for the nanoalloy under consideration is $3 \pm \delta : 1$. This result has been obtained using bulk-sensitive techniques, therefore differences with previous estimates can be assigned to variations in the stoichiometry at the surface of the grains possibly measured by techniques more sensitive to the surfaces. Moreover, differently prepared batches of samples with similar nominal composition are known to show large variations in mean sizes (and likely also in stoichiometry), so results are in line with previous observations. Based on these results, in subsequent sections the nanomaterial under consideration is indicated as $Pt_{3\pm\delta}$Co-Vulcan, and therefore a thin film of $Pt_{3\pm\delta}$Co alloy, prepared by molecular beam epitaxy,[32] has been taken as a reference.

III. XAS DATA ANALYSIS: METHODOLOGY AND APPLICATION TO $Pt_{3\pm\delta}$Co SAMPLES

A. XAS measurements

In order to perform XAS measurements in transmission mode a pellet was prepared by carefully mixing the $Pt_{3\pm\delta}$Co-Vulcan powder and graphite, producing a sample with average metal thickness chosen to give an optimal jump both at the Pt L_3 absorption edge ($J \sim 0.8$) and at the Co K absorption edge ($J \sim 0.2$). High-quality Pt L_3-edge and Co K-edge XAS spectra [see Fig. 3(b)] were collected at the Synchrotron Light Laboratory ELETTRA (XAFS station, Trieste, Italy) using a double-crystal monochromator equipped with Si(111) crystal (see Ref. 33 for details). Measurements were performed at room temperature and the raw XAS data are presented in Fig. 3.

In Fig. 3(a), we report the near-edge XAS spectra of the Pt L_3 and Co K edges after removal of the pre-edge absorption (without normalization to the absorption jump). The Pt : Co stoichiometry and Co atomic fraction f_{Co}, calculated on the basis of Pt and Co absorption discontinuities, are presented in Table I. Figure 3(b) shows a direct comparison between experimental $\chi(k)$ signals of $Pt_{3\pm\delta}$Co-Vulcan nanoalloy and $Pt_{3\pm\delta}$Co thin film.[32] The difference in the intensity of the XAS signals, due to the nanocrystalline nature of the $Pt_{3\pm\delta}$Co-Vulcan nanoalloy, is discussed in the next section.

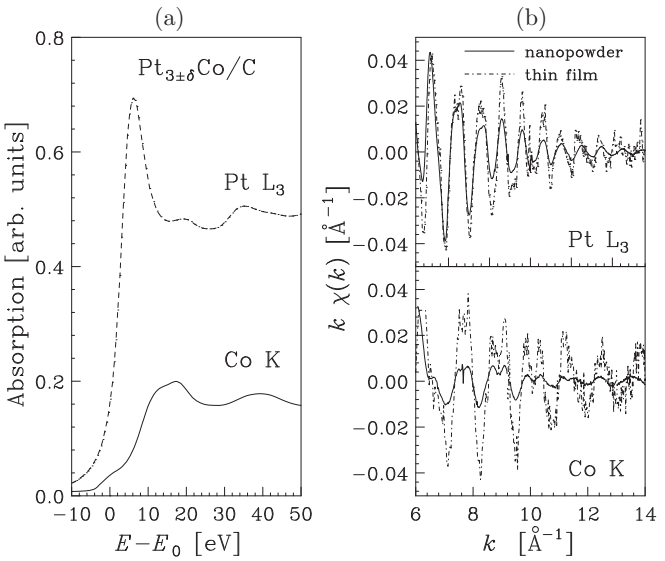

FIG. 3. (a) Comparison of Pt L_3 and Co K near-edge XAS spectra of $Pt_{3\pm\delta}$Co-Vulcan powder. E_0 is the edge energy. (b) Experimental $\chi(k)$ signals of $Pt_{3\pm\delta}$Co-Vulcan nanopowder and $Pt_{3\pm\delta}$Co thin film. Top panel shows Pt L_3 edge, bottom panel shows Co K edge.

B. Data analysis method

Our TEM and XRD results shows that the $Pt_{3\pm\delta}$Co-Vulcan sample can be considered as constituted by a homogeneous ensemble of $Pt_{3\pm\delta}$Co fcc nanocrystalline particles with a mean diameter of ∼5 nm. The observed strong reduction in the amplitude of the structural signal $\chi(k)$ [see Fig. 3(b)] is associated mainly with a reduction of the mean coordination numbers (CNs; contribution of ill-coordinated atoms from the surface of nanoparticles) and to an increase of structural disorder.[13]

XAS, TEM, and XRD data indicate that the average local structure of $Pt_{3\pm\delta}$Co-Vulcan nanoalloy can be safely assumed to be very similar to that of bulk crystalline Pt_3Co (as for Pt nanoparticles[13]). Therefore, a good starting model for performing a detailed XAS structural analysis is that of bulk Pt_3Co. The Pt_3Co alloy has an $L1_2$ structure (Cu_3Au-like).[30] In this structure Co substitutes Pt atoms at the corners of the crystal structure of the face-centered-cubic (fcc). Details of the $L1_2$ structure are presented in Tables II and III.

TABLE II. Two-atom (g_2) configurations in a typical fcc $L1_2$ structure: R_1 is the mean distance between atoms Pt-M (M = Pt or Co), R_2 is the mean distance between atoms Co-M (M = Pt or Co), and N_C is the number of neighbors M.

Atoms	Shell	Nc	R_1 [Å]	Atoms	Shell	Nc	R_2 [Å]
Pt-Pt	I	8	2.70	Co-Pt	I	12	2.70
Pt-Co	I	4	2.70	Co-Co	I		
Pt-Pt	II	6	3.83	Co-Pt	II		
Pt-Co	II			Co-Co	II	6	3.83
Pt-Co	III	8	4.69	Co-Pt	III	24	4.69
Pt-Pt	III	16	4.69	Co-Co	III		
Pt-Pt	IV	12	5.41	Co-Co	IV	12	5.41

TABLE III. Three-atom (g_3) configurations in a typical fcc $L1_2$ structure for Pt L_3 and Co K edges. R_{0_1} and R_{0_2} are the mean distances of two shortest bonds with angle Θ in between. Freq. (frequency) is half of the length of the triangle perimeter, corresponding to the peak leading frequency in the Fourier spectrum. Deg. is the degeneracy specified for each configuration, with the photoabsorber placed at the vertex between the two shortest bonds (e.g., Pt-Co-Co: Pt atom is at the vertex). ph$N$ indicates that the photoabsorber is positioned in position N (side of the triangle, not the triangle vertex).

Atoms Type	Deg.	$R_{0_1} = R_{0_2}$ [Å]	R_{0_3} [Å]	Θ [deg]	Freq. [Å]
		Pt L_3			
Pt-Co-Pt	16	2.70		60	4.06
Pt-Pt-Pt	8	2.70		60	4.06
Pt-Pt-Pt	8	2.70		90	4.62
Pt-Pt-Pt (ph2)	16	2.70	Pt-Pt II shell	90	4.62
Co-Pt-Pt (ph2)	8	2.70	Pt-Pt II shell	90	4.62
Pt-Co-Co	4	2.70		90	4.62
Pt-Pt-Pt	8	2.70		120	5.05
Pt-Pt-Pt	16	2.70	Pt-Pt III shell	120	5.05
Pt-Pt-Co	16	2.70		120	5.05
Pt-Pt-Co (ph2)	16	2.70	Pt-Co III shell	120	5.05
Co-Pt-Pt (ph2)	16	2.70	Pt-Pt III shell	120	5.05
Pt-Pt-Pt	4	2.70		180	5.41
Pt-Pt-Pt (ph2)	8	2.70	Pt-Pt IV shell	180	5.41
Co-Pt-Pt (ph2)	4	2.70	Pt-Pt IV shell	180	5.41
Pt-Co-Co	2	2.70		180	5.41
		Co K			
Co-Pt-Pt	24	2.70		60	4.06
Pt-Co-Co (ph2)	24	2.70	Co-Co II shell	90	4.62
Co-Pt-Pt	12	2.70		90	4.62
Co-Pt-Pt	24	2.70		120	5.05
Pt-Pt-Co (ph3)	48	2.70	Co-Pt III shell	120	5.05
Co-Pt-Pt	6	2.70		180	5.41
Pt-Co-Co (ph2)	12	2.70	Co-Co IV shell	180	5.41

The experimental EXAFS data have been analyzed using theoretical calculations of the x-ray absorption cross section in the framework of the GNXAS method.[14,15]

In previous papers, the GNXAS method was applied to various nanocrystalline systems showing the importance of accounting for induced defects in those obtained by high-energy ball milling,[2] and the role of multiple scattering in those[2] and other nanophase[3,13] systems. For these reasons, Pt L_3-edge and Co K-edge EXAFS experimental data obtained for the considered $Pt_{3\pm\delta}$Co systems have been analyzed using MS contributions through n-body γ signals.

The two-body and three-body ($\gamma^{(2)}$ and $\gamma^{(3)}$ associated with pair and triplet atomic configurations; hereinafter called g_2 and g_3 peaks) have been calculated starting from the model fcc structure using nonoverlapping potentials within the muffin-tin approximation ($R_{\rm MT}^{\rm Pt} = 1.39$ Å and $R_{\rm MT}^{\rm Co} = 1.25$ Å for a first-neighbors distance $R_{\rm FN} \approx 2.70$ Å). The complex Hedin-Lundqvist energy-dependent potential has been used, for which the inelastic mean-free path (MFP) of the excited photoelectron, $\lambda(E)$, has been calculated automatically and the core hole lifetime has been defined as a constant parameter taken from Ref. 34. The XAS signal has been calculated for various two-body and three-body configurations of a typical

fcc $L1_2$ structure. Due to the limited electron MFP and atomic vibrations, at room temperature, the main frequency components contributing to the measured $\chi(k)$ signal are limited within a sphere of about 6 Å around the photoabsorbing atoms.

The $\gamma^{(2)}$ and $\gamma^{(3)}$ signals have been averaged for configurational disorder using Gaussian functions for both g_2 and g_3 peaks. The structural refinement has been performed by minimizing the difference between the raw absorption data and the model data computed by multiplying the structural oscillation, $\chi(k)$, by a suitable background normalizing factor, which is a standard practice with GNXAS.[15] It is important to remark that the chosen atomic background includes contributions of many-electron channels, usually amounting up to a few percent of the absorption cross section. As widely discussed elsewhere, inaccurate modeling of the atomic background can result in the presence of low-frequency components without structural origin in the XAS structural signal. In this study for our $Pt_{3\pm\delta}Co$ samples, a background shape has been modelled taking into account specific double-electron excitation effects: two additional excitation channels ($2p\ 4f$) and ($2p\ 4p$) for the Pt L_3 edge (about 110–130 and 500 eV after the absorption edge, respectively), and ($1s\ 3s$) or ($1s\ 3p$) for the Co K edge (about 110–130 eV after the absorption edge), in agreement with previous studies.[13,32]

C. Effect of chemical disorder: computer simulations

Chemical disorder is known to be present in crystalline platinum cobalt alloys, depending obviously on the preparation procedures and thermal treatment. Here we have used a simple methodology for introducing the effect of substitutional disorder in the calculation of the coordination numbers (CNs) and multiplicities of the multiple-scattering signals contributing to the EXAFS spectra.

In fact, the introduction of chemical disorder obviously changes Pt-Co, Co-Pt, Co-Co, and Pt-Pt first- and further-neighbor CNs, as compared with the ordered structure. For this reason, we have calculated the multiplicities of the main local two-body and three-body fcc $L1_2$ configurations as a function of the degree of chemical disorder (see also Ref. 35), introducing occupation probabilities of the lattice sites within a simple computer simulation scheme. To the purpose of minimizing the effects of the finite size of our calculations, we have considered a $6 \times 6 \times 6$ supercell containing 216 fcc units ($a = 3.385$ Å) for a total number of 864 atoms.

Substitutional disorder is simulated by introducing a finite probability $0 \leqslant p \leqslant 1$ for the occupancy of selected lattice sites with Co atoms. In particular, p is taken as the probability that a Co atom occupies the site at the corner of the fcc cell [(0,0,0) position in each fcc unit, see Fig. 4(a)]. Conversely, $(1-p)/3$ is taken as the Co occupation probability of any of the three other sites of the fcc unit [(1/2,1/2,0), (0,1/2,1/2), (1/2,0,1/2) positions]. This assumption allows us to preserve the stoichiometry in the thermodynamic limit. In our calculations we considered the range $0.25 < p < 1$, spanning from a completely ordered structure ($p = 1$) to a completely disordered one ($p = 0.25$, for which no preferential position can be defined for Co).

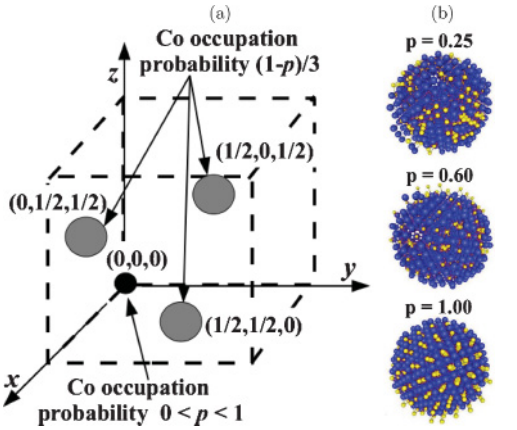

FIG. 4. (Color online) (a)$L1_2$ primitive cell; the arrows indicate the Co occupation probability for every site. (b) Three different spherical nanocrystals with a fcc $L1_2$ structure and with a different degree of chemical disorder.

A suitable order parameter is defined as

$$s = \frac{p - C_a}{1 - C_a}, \tag{2}$$

were p is the occupation probability defined above, C_a is the atomic concentration of the selected chemical species (1/4 for Pt_3Co). Thus, $s = 0$ indicates random occupancy ($p = 1/4$) and $s = 1$ indicates perfect order.

Calculations averaged on 3000 different supercells were performed for 16 different s values corresponding to 16 degrees of chemical disorder. The s range was selected from 0 to 1 with a step $\Delta s = 0.0625$. In Fig. 4(b) three examples of spherical clusters (obtained using selected cutoff radii for the supercells) and different chemical ordering s are shown. Obviously, it must be remarked that the determination of a realistic model reproducing the atomic structure and dynamics in nanocrystalline materials including grain boundaries is beyond the scope of the present work.

In Fig. 5 we report the results of the calculated first-, second-, third-, and fourth-shell g_2 CNs as a function of the order parameter s for bulk fcc Pt_3Co. For nanoparticles, the reduction in CNs due to the finite size has been taken into account using previous simulations performed for fcc nanoparticles.[13] For example, in particles with a mean size of about 5 nm the total first-neighbor CN is ~11 instead of 12.

The evaluation of the average degeneracy of the three-body configurations in a chemically disordered binary alloy is a more difficult and time-consuming task. For this reason, a reliable estimation of the three-body degeneracy $N_3(s)$, as a function of order parameter s, was obtained using the following expression:

$$N_3(s) = \frac{N_{0_1}(s) N_{0_2}(s)}{2} f_{\text{conf}}(s). \tag{3}$$

Here, $N_{0_1}(s)$ and $N_{0_2}(s)$ are the two-body CNs related to the shortest chemical bonds. For example, in a triangular Pt-Co-Co configuration, the Pt atom is at the triangle vertex, and Pt-Co are the two shortest bonds, so $N_{0_1}(s)$ and $N_{0_2}(s)$ are, in this case, the $Pt_{3\pm\delta}Co$ first-neighbor CNs. In Eq. (3), $f_{\text{conf}}(s)$ is a geometrical parameter typical for each three-body fcc

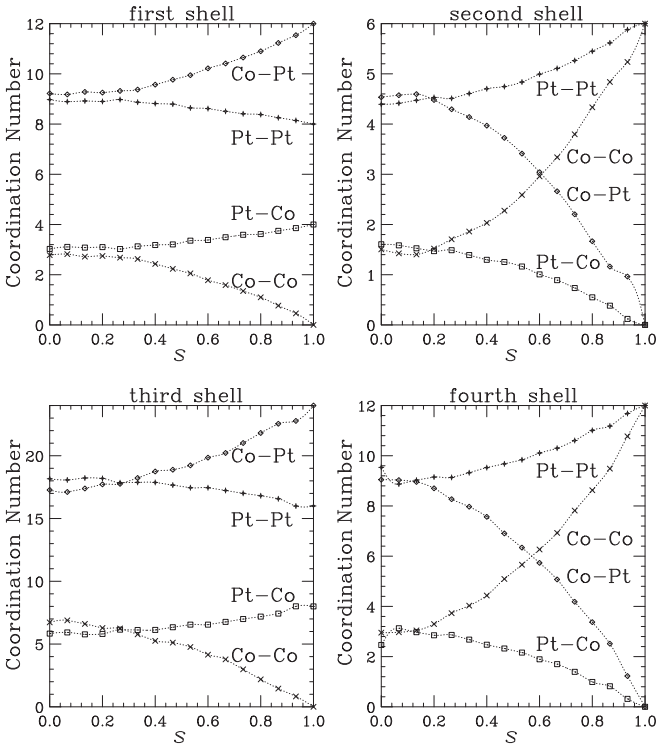

FIG. 5. Two-body coordination numbers as a function of the s (chemical order) parameter for a bulk fcc alloy, calculated in this work. The top-left, top-right, bottom-left, and bottom-right panels show the first, second, third, and fourth g_2 shells, respectively.

configuration, which is assumed to depend smoothly on the s chemical order parameter.

The limiting case of absence of chemical order ($s = 0$), useful for estimating limiting values for the degeneracy of three-body terms and of two-body distant shells, can be simply calculated assuming that the occupancy fraction on each site is just proportional to the atomic fraction (stoichiometry).

The occurrence probability of a three-leg configuration A-AA, A-AB, or A-BB, centered on atom A, for a given AB alloy, turns out to be just proportional to the products of the occupancy fractions (in the case of this calculation A_3B: $f(\mathrm{B}) = 1/4$ and $f(\mathrm{A}) = 3/4$). So we have $f(\mathrm{AA}) = 9/16$, $f(\mathrm{AB}) = 6/16$ (AB and BA count twice), and $f(\mathrm{BB}) = 1/16$, with the sum obviously equal to 1. Using this result and considering the actual total number of configurations associated with a particular geometry (fcc structure in this case), we can calculate the asymptotic degeneracy value for a chemically disordered system ($s = 0$). By knowledge of the two limiting values $f_{\mathrm{conf}}(s = 0)$ and $f_{\mathrm{conf}}(s = 1)$, and assuming a linear dependence on the chemical disorder, the $f_{\mathrm{conf}}(s)$ can be calculated for each three-body configuration as a function of s.

The degeneracy $N_3(s)$ for each three-body configuration as a function of chemical disorder are then estimated by Eq. (3). In Fig. 6, as an example, the $N_3(s)$ degeneracy trends are shown versus order parameter obtained for g_3 configurations with 180° vertex angle. Similar trends are obtained for different triangular configurations.

Looking at the results presented in Figs. 5 and 6 it is clear that chemical disorder has a deep influence on CNs

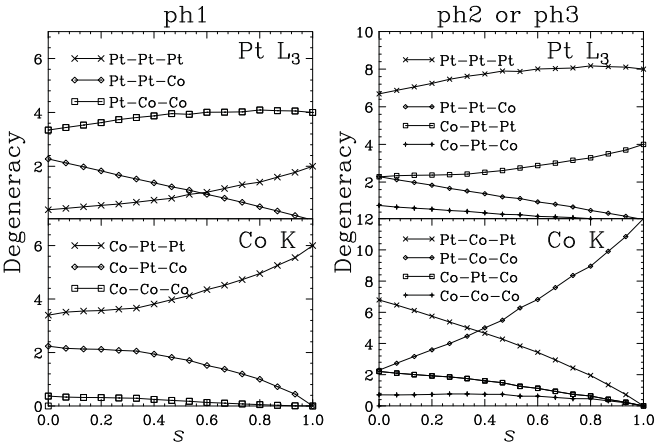

FIG. 6. Calculated degeneracy for three-body configurations with 180° vertex angle (bulk fcc alloy) as a function of s (chemical order) parameter. The left panel shows the photoabsorber at position ph1 (vertex with 180° angle) and the right panel shows the photoabsorber at position ph2 or ph3 (other two sites in the triangle).

and degeneracy associated with the amplitude of the MS XAS signals. In particular, some CNs drop to zero for the fully ordered structure while most CNs and degeneracy are slowly varying for s lower than 0.3. In particular, the large changes in the CNs and degeneracy of the fourth-shell atoms (180° configurations) are identified as possible flags for chemical ordering in these alloys (along with the presence of Co-Co first neighbors). This is shown in Fig. 7, where we report the Fourier transforms (FTs) of the Pt L_3- and Co K-edge theoretical XAS signals calculated for different values of the disorder parameter s (using best-fit structural parameters obtained for the first four neighbor shells of the nanoalloy system; see next sections). The Co K-edge

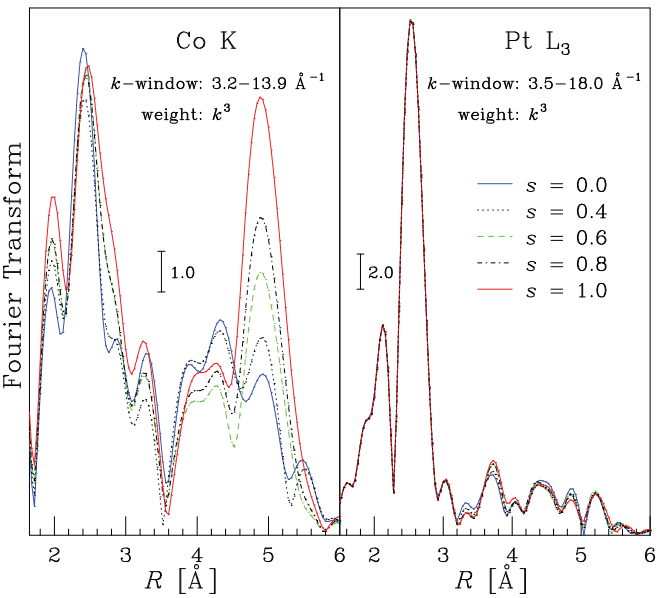

FIG. 7. (Color online) Fourier transforms of the Pt L_3 and Co K theoretical XAS signals calculated for different values of the disorder parameter s (structural parameters optimized for the $Pt_{3\pm\delta}Co$ nanoalloy).

FT is found to be especially sensitive to chemical disorder and, in particular, the intensity of the FT peak around 5 Å associated with collinear configurations changes by a factor of 3 between the limiting cases $s = 0$ and $s = 1$.

IV. XAFS ANALYSIS RESULTS AND DISCUSSION

A. $Pt_{3\pm\delta}Co$ thin film

In this section a double-edge (Co K and Pt L_3) analysis of EXAFS signals associated with a crystalline $Pt_{3\pm\delta}Co$ thin film is presented (for original data and first-shell analysis see Ref. 32). The MS analysis of the EXAFS spectra presented here is related to a thin film grown by molecular beam epitaxy (MBE) at 800 K.[32] The formal stoichiometry of this film is $Pt_{\sim 2.3(3)}Co$ and is within the stability range of the fcc $L1_2$ structure (see Ref. 32 and references therein). However, the film exhibits only partial $L1_2$-type ordering. The stacking fcc sequence contains some stacking faults and chemical disorder.

Taking as a reference the bulk Pt_3Co crystalline structure (fcc $L1_2$ lattice), the expected atomic configurations contributing to the EXAFS signals (confined within 5–6 Å due to the short-range nature of the technique) are those presented in Tables II and III. However, the presence of a partial chemical disorder (namely, a finite probability for having Co atoms instead of Pt atoms, and vice versa, into the regular lattice sites) leads to the inclusion of additional structural configurations in the model for the structural refinement. In fact, various two-body and three-body contributions are absent in the chemically ordered structure $s = 1$ but must be introduced in presence of chemical disorder (for example, Co-Co for first- and third-shell configurations and Co-Pt for second and fourth shells, see Fig. 5).

Our modeling of the local structure includes the following two- and three-body contributions (see also Fig. 8):

(1) First neighbors. The first-shell total two-body signals $\gamma_1^{(2)}$ for Pt-Pt, Pt-Co, Co-Co, and Co-Pt were modeled as Gaussian distributions with three parameters: average distance R, variance σ^2, and coordination number. CNs are a function of a chemical disorder of the lattice and we allowed variations of these values, according to the chemical order parameter s by imposing the overall constraint that the total value of both sums Pt-Co with Pt-Pt and Co-Co with Co-Pt must be equal to 12. The number of floated structural parameters related to these contributions is 7.

(2) Second, third, and fourth neighbors. We accounted for both two-body and three-body signals using Co-Co-Co, Co-Co-Pt, Co-Pt-Pt, and Pt-Pt-Pt triangular configurations formed by two first-neighbor bonds and bond angles of 90°, 120°, and 180° (fixed values). CNs and degeneracy of the triangular configurations have been floated according to the chemical order parameter s (see Figs. 5 and 6). We used diagonal covariance matrices for the thermal average so introducing only the bond-angle-variance σ^2_Θ as an additional parameter.[15,36] The collinear contribution (180°) related to the fourth shell is, as expected, the stronger one (see Fig. 8) and, in this case, it has been necessary to introduce explicitly the bond-bond correlation parameter $\rho_{r,r'}$.[15] The number of additional floating parameters is only 4 resulting in a total of 11 structural parameters for this double-edge EXAFS refinement.

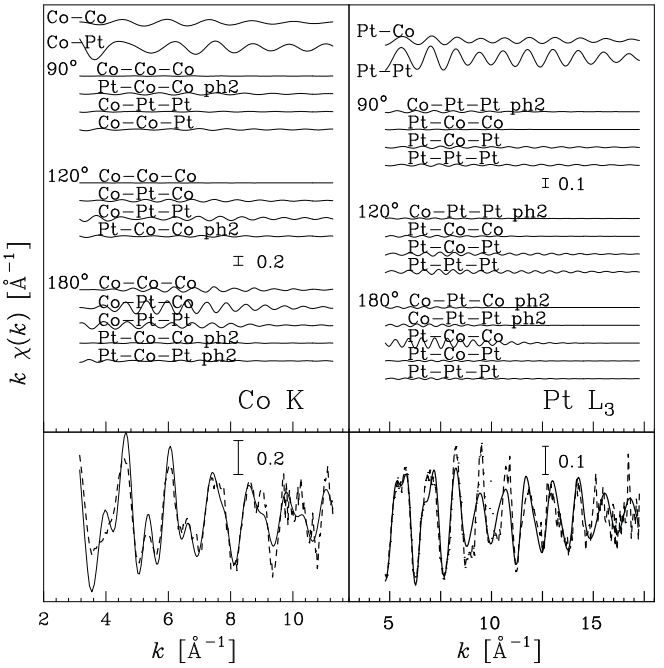

FIG. 8. The best double-edge-fit results of a GNXAS analysis performed for $Pt_{3\pm\delta}Co$ thin film at Co K edge (left) and Pt L_3 edge (right). Upper curves represent components of the model signal, vertically shifted for clarity. The solid line is the model signal and the dashed line is the experimental signal. The scale is indicated within the figure.

As shown in Fig. 8, MS best-fit calculations obtained within the above-mentioned approximations provide an accurate fitting of the experimental data for both Co K and Pt L_3 edges.

The best-fit structural parameters of all the considered two-body configurations obtained by GNXAS analysis of the $Pt_{3\pm\delta}Co$ thin film are reported in Table IV. The parameters defining the first-shell distributions (i.e., R and σ^2 for shell I in Table IV) are those measured with higher accuracy as they are related both to the direct first-neighbor two-body signal and to several MS contributions. Bond-angle standard deviations were found in a range around 1°–3° while the bond-bond correlation of the collinear configuration was negative, $\rho_{r,r'} \sim -0.3$, as found in other fcc systems.

Best-fit first-neighbor structural results are in good agreement with those of a previous analysis made by C. Meneghini *et al.* [32] Moreover, the bond variance σ^2 is in good agreement with previous calculations performed for monoatomic crystals (cf. $\sigma^2 = 0.004$–0.005 Å^2 for Pt-Pt first shell signal[37] and 0.005–0.006 Å^2 for Co-Co first shell signal[38]). The same holds for the second and further shells, for which the distance variances are found to approach the uncorrelated limit $2u^2 \approx 0.01$ Å^2 (u^2 is the fluctuation around equilibrium positions).

As discussed before, the main effect of chemical disorder is a change in the coordination numbers and degeneracy of the MS signals reproducing the experimental EXAFS spectrum (see Figs. 5 and 6). The coordination numbers and three-body degeneracy obtained for this $Pt_{3\pm\delta}Co$ thin film are compatible with a chemical order parameter s ranging from 0.0 to 0.4. In fact, the amplitudes of the MS signals are very weakly dependent on the variation of the order level in this limit. The

TABLE IV. Structural parameters of the two-body configurations obtained by GNXAS analysis for $Pt_{3\pm\delta}Co$ thin film. R is the average interatomic distance, σ^2 is the distance variance, and N_c is the coordination number. Estimated errors are shown in brackets on the last digits. The order parameter was found to be $s \in [0.0,0.4]$.

$Pt_{3\pm\delta}Co$ thin film				
Atoms	Shell	N_c	R [Å]	σ^2 [Å^2]
Pt-Co	I	3.2	2.706(5)	0.0045(5)
Pt-Pt	I	8.8	2.725(5)	0.0040(5)
Pt-Co	II[a]	1.5	3.80(1)	0.0055(7)
Pt-Pt	II[a]	4.5	3.83(2)	0.0052(7)
Pt-Co	III[a]	6.0	4.70(3)	0.007(1)
Pt-Pt	III[a]	18.0	4.70(2)	0.0067(2)
Pt-Co	IV[a]	2.5	5.43(4)	0.009(1)
Pt-Pt	IV[a]	9.5	5.42(4)	0.0092(8)
Co-Co	I	2.4	2.65(1)	0.0045(8)
Co-Pt	I	9.6	2.706(5)	0.0044(5)
Co-Co	II[a]	2.3	3.827(1)	0.0056(9)
Co-Pt	II[a]	3.7	3.80(1)	0.0055(7)
Co-Co	III[a]	5.0	4.68(2)	0.0073(9)
Co-Pt	III[a]	19.0	4.70(3)	0.007(1)
Co-Co	IV[a]	4.1	5.30(6)	0.009(2)
Co-Pt	IV[a]	7.9	5.43(4)	0.009(1)

[a]Parameter derived from the three-atom configuration.

thin film is thus found to be chemically disordered, as also indicated in a previous study[32] where only first-shell signals have been taken into consideration.

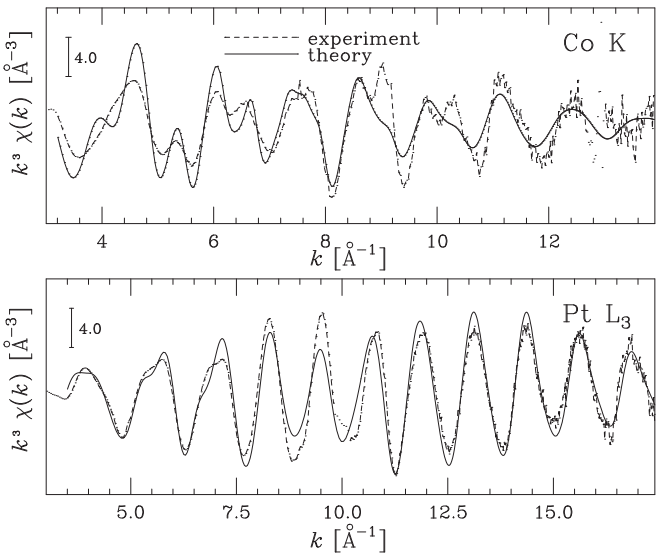

FIG. 9. The best-fit results of GNXAS analysis performed for $Pt_{3\pm\delta}Co$-Vulcan (E-TEK^{TM}) at Co K edge (top) and Pt L_3 edge (bottom) (k^3 weighted). The dashed line is the experimental signal and the solid line is the sum of all theoretical components of the signal (individual components are shown in the case of the $Pt_{3\pm\delta}Co$ thin film analysis; see Fig. 8).

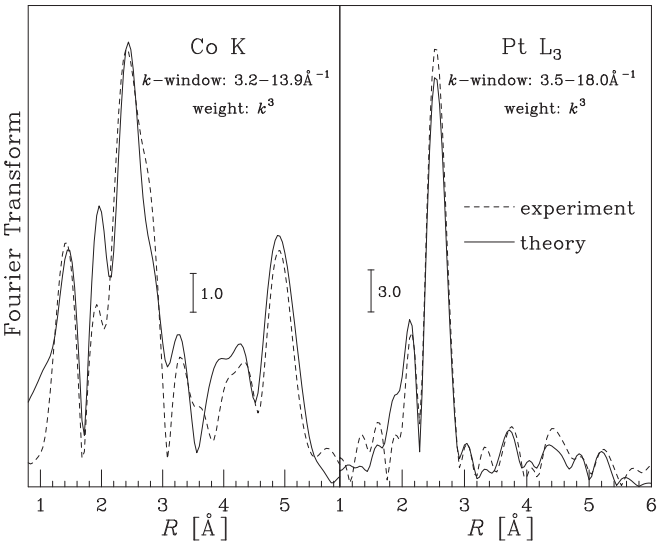

FIG. 10. Fourier transforms of the EXAFS experimental signals collected at Co K edge (left) and Pt L_3 edge (right) for $Pt_{3\pm\delta}Co$-Vulcan compared with theoretical signals calculated with chemical disorder parameter $s = 0.6$.

B. $Pt_{3\pm\delta}Co$ nanoparticles

A detailed double-edge (Co K and Pt L_3) analysis has also been performed for $Pt_{3\pm\delta}Co$-Vulcan (E-TEK^{TM}) powder, using the GNXAS method in combination with XRD and TEM results, accounting for the actual nanoparticles size distribution and morphology. This is very important for structural analysis, because the nanometric size of the particles (the presence of surface ill-coordinated atoms, depending on size and shape of the grains) strongly affects the multiplicities of the typical MS signals associated with the two-body and three-body configurations.

The same methods for calculation and selection of the MS XAS signals described in the preceding Sec. IV A have been used for $Pt_{3\pm\delta}Co$-Vulcan nanocrystallites. Some important additional constraints and new features have been taken into account:

(1) total coordination numbers and degeneracy of the MS signals have been floated within a range compatible by the measured size distribution of the nanoparticles;

(2) values of distance and angle variances (σ^2) obtained for the $Pt_{3\pm\delta}Co$ thin film have been taken as lower limits of the corresponding distributions in $Pt_{3\pm\delta}Co$-Vulcan nanocrystallites;

(3) the background model and other important nonstructural parameters (i.e., overall amplitude factor S_0^2 and energy E_0[15]) were fixed to the values used for the $Pt_{3\pm\delta}Co$ thin film EXAFS refinement;

(4) the presence of a moderate amount of cobalt oxide was found to be necessary for an accurate refinement of the Co K-edge EXAFS spectrum.

These constraints have been found to guarantee a robust double-edge structural refinement of the nanocrystalline $Pt_{3\pm\delta}Co$-Vulcan sample, using a total of 15 structural parameters, over around 1000 experimental points, and including all of the MS signals up to the fourth coordination shell.

The GNXAS analysis results are presented in Figs. 9 and 10 and the structural parameters obtained for two-body

configurations (up to the fourth coordination shell) are shown in Table V.

Comparing XAS spectra of $Pt_{3\pm\delta}Co$ thin film to $Pt_{3\pm\delta}Co$-Vulcan nanocrystallites [see Fig. 3(b)] the main visible difference is a reduction of the $\chi(k)$ signal amplitude, in particular for Co K edge. This is mainly caused (as mentioned before) by a decrease in the average CNs (degeneracy) due to the average particle size, but the peculiar intensity reduction of the Co K-edge EXAFS can be explained only by structural and chemical disorder affecting the Co sites.

Increase of structural and chemical disorder and reduction of CNs are strongly correlated quantities, but act differently on the MS signals due to their different k dependence, so their decoupling was possible by fitting the raw (double-edge) data in a large energy range without any Fourier filtering.

Two main results can be inferred looking at the distance distributions obtained by EXAFS refinement. First, the best-fit structural parameters reported in Table V show, without ambiguity, that the distributions of distances measured by the variances σ^2 are much broader than those obtained for the thin film $Pt_{3\pm\delta}Co$ (cf. Table IV), especially for those concerning the Co sites. The anomalous disordering of Co sites explains most of the differences in amplitude found for the nanocrystalline system as compared with the thin film [see Fig. 3(b)]. Second, there is a contraction of the average interatomic distances as compared with the thin film (around 0.03 Å). Only for first-shell Co-Co configuration is an increase of a bond length observed. Stoichiometry effects leading to contraction can be excluded both because they are known to affect the first-shell distances in an almost negligible way, and because the nanocrystalline system is slightly richer in Pt content (which would rather increase the average distances). The contraction of the bond lengths, already observed in other nanosized systems, is mainly the effect of the presence of surface-like atoms, whose bonds are oriented only toward the inner atoms of the crystal grain.

The CNs and three-body degeneracies obtained for the nanocrystalline $Pt_{3\pm\delta}Co$ sample are compatible with a chemical order parameter $s = 0.6(1)$ (see Figs. 5 and 6). The $Pt_{3\pm\delta}Co$ nanoalloy turns out to be slightly more chemically ordered than the corresponding thin film.

The mean particle size could also be estimated by directly using EXAFS data and the curves depicted in Ref. 13. Considering the quasispherical shape of $Pt_{3\pm\delta}Co$ particles, we obtain CNs corresponding to a mean particle size of 4.7 ± 1.0 nm, which is consistent with results obtained by TEM and XRD (see Table I).

The x-ray diffraction pattern (see Fig. 2) did not reveal the presence of pure crystalline cobalt or cobalt oxide in the sample. Therefore, the presence of a moderate fraction of cobalt oxide in the nanoalloy deserves finally some discussion. A limited number of Co-O bonds, indicated by the small Co-O coordination number ($N_{CoO} \sim 1.1$, see Table V), has been found by EXAFS. This is accompanied also by a slight excess of Co atoms detected by XAS with respect to the XRD-extracted stoichiometry (about 10%, see Table I). These observations suggest that the excess of Co atoms is found mainly in the oxidized form (some Co fraction is not alloyed with Pt). We can speculate that the nanoparticles in a considered sample may consist of a Pt_3Co crystalline core (with a mean diameter of about 4.3 nm) with a Pt-rich skin (a few atomic monolayers) where Co at the surface is possibly oxidized. The idea of a different stoichiometry at the surface, leading to a skin of Pt-rich alloy is compatible with other results (see, e.g., Ref. 17 and references therein).

TABLE V. Best fit results for the two-body configurations obtained by GNXAS analysis for $Pt_{3\pm\delta}Co$-Vulcan nanoparticles: R is the average interatomic distance, σ^2 is the distance variance, N_c is the coordination number. Estimated errors are shown in brackets on the last digits. The order parameter was found to be $s = 0.6(1)$.

$Pt_{3\pm\delta}Co$ nanoparticles				
Atoms	Shell	N_c	R [Å]	σ^2 [Å^2]
Pt-Co	I	3.4	2.684(5)	0.012(1)
Pt-Pt	I	7.6	2.703(5)	0.0063(8)
Pt-Co	II[a]	0.4	3.80	0.014
Pt-Pt	II[a]	4.8	3.80	0.009
Pt-Co	III[a]	5.4	4.67	0.015
Pt-Pt	III[a]	14.4	4.67	0.014
Pt-Co	IV[a]	0.7	5.37	0.025
Pt-Pt	IV[a]	10.6	5.39	0.019
Co-Co	I	1.1	2.689(8)	0.014(3)
Co-Pt	I	9.9	2.684(5)	0.012(1)
Co-O		1.1	1.86(1)	0.0029(7)
Co-Co	II[a]	3.6	3.80	0.013
Co-Pt	II[a]	1.7	3.80	0.014
Co-Co	III[a]	2.1	4.65	0.018
Co-Pt	III[a]	18.2	4.67	0.015
Co-Co	IV[a]	4.5	5.37	0.025
Co-Pt	IV[a]	4.7	5.37	0.025

[a]Parameters derived from the three-atom configuration.

V. CONCLUSIONS

In this work, the local structure of $Pt_{3\pm\delta}Co$ nanoalloy has been investigated by XAS double-edge multiple-scattering GNXAS refinement, using pair and triplet contributions associated with distances and bond angles up to the fourth coordination shell. Stoichiometry and size distribution of the nanoparticles has been obtained by combining TEM, XRD, and XAS results. This information has been used in the detailed EXAFS refinement of the local structure. The EXAFS spectrum of a thin film of bulk-like $Pt_{3\pm\delta}Co$ alloy has been analyzed showing that chemical ordering plays a significant role in determining the intensity of the structural signal. Computer simulations based on a simple model accounting for substitutional disorder have been carried out calculating the variation of the intensity of the individual pair and triplet contributions to the XAS spectra, as a function of an order parameter s ($s = 0$ indicates random occupancy of lattice sites and $s = 1$ indicates perfect ordering). It has been found that individual XAS contributions related to the minority species (Co) are extremely sensitive to substitutional disorder so the intensity of those signals can be used as a reliable measure

of the ordering level of the alloy. The thin film alloy has been found to be chemically disordered ($s \leqslant 0.4$), in agreement with previous estimates. The $Pt_{3\pm\delta}Co$ nanoalloy has been found to be partially ordered: $s = 0.6 \pm 0.1$. Chemical disordering was found to be measured with high accuracy especially by the XAS signal associated with collinear triplet configurations including Co atoms. We also found that the local structure around Co atoms is characterized by a higher level of structural disorder, as compared to Pt, monitored by the higher variances in interatomic distances. Moreover, we have found evidence of cobalt-oxygen bonds probably located at the surface of the grains but no traces of oxidation of Pt; a fact that may assist the catalytic activity of this material.

This successful application leads us to conclude that the robust approach for nanomaterial characterization here presented, combining different state-of-the-art techniques, is suitable for applications in structural refinements of any binary nanocrystalline functional system, including those for energy-related applications.

ACKNOWLEDGMENTS

We gratefully acknowledge the support of the Synchrotron Light Laboratory ELETTRA and the entire beamline staff: L. Olivi, A. Cognigni, and N. Novello (XAFS 11.1 station). We would like to thank E. Larquet and N. Menguy (IMPMC, Pierre et Marie Curie University, Paris) for their invaluable help during the TEM and HRTEM measurements. We also thank C. Meneghini for providing the original data of the thin film sample. This research is partly associated with the NUME Project "Development of composite proton membranes and of innovative electrode configurations for polymer electrolyte fuel cells" (MIUR, FISR 2003). G. Greco gratefully acknowledges the Italian CNISM for supporting her grant and travel expenses.

*giorgiagreco80@gmail.it
†agnieszka@mif.pg.gda.pl

[1] Various authors, in *X-Ray Absorption Fine Structure For Catalysts and Surfaces*, edited by Y. Iwasawa (World Scientific, Singapore, 1996), pp. 375–384.
[2] A. Di Cicco, M. Berrettoni, S. Stizza, E. Bonetti, and G. Cocco, Phys. Rev. B **50**, 12386 (1994).
[3] F. Boscherini, S. de Panfilis, and J. Weissmüller, Phys. Rev. B **57**, 3365 (1998).
[4] A. I. Frenkel, C. W. Hills, and R. G. Nuzzo, J. Phys. Chem. B **105**, 1115 (2001).
[5] V. Stamenkovic, T. J. Schmidt, P. N. Ross, and N. M. Markovic, J. Phys. Chem. B **106**, 11970 (2002).
[6] U. A. Paulus, A. Wokaun, G. G. Scherer, T. J. Schmidt, V. Stamenkovic, N. M. Markovic, and P. N. Ross, Electrochim. Acta **47**, 3787 (2002).
[7] H. A. Gasteiger, S. S. Kocha, B. Sompalli, and F. T. Wagner, Appl. Catal., B **56**, 9 (2005).
[8] S. Mukerjee, S. Srinivasan, M. P. Soriaga, and J. McBreen, J. Phys. Chem. **99**, 4577 (1995).
[9] T. Toda, H. Igarashi, H. Uchida, and M. Watanabe, J. Electrochem. Soc. **146**, 3750 (1999).
[10] M. k. Min, J. Cho, K. Cho, and H. Kim, Electrochim. Acta **45**, 4211 (2000).
[11] F. H. B. Lima, M. J. Giz, and E. A. Ticianelli, J. Braz. Chem. Soc. **16**, 328 (2005).
[12] F. H. B. Lima, J. R. C. Salgado, E. R. Gonzalez, and E. A. Ticianelli, J. Electrochem. Soc. **154**, A369 (2007).
[13] A. Witkowska, A. Di Cicco, and E. Principi, Phys. Rev. B **76**, 104110 (2007).
[14] A. Filipponi, A. Di Cicco, and C. R. Natoli, Phys. Rev. B **52**, 15122 (1995).
[15] A. Filipponi and A. Di Cicco, Phys. Rev. B **52**, 15135 (1995).
[16] C. Leroux, M. C. Cadevillet, V. Pierron-Bohnes, G. Indent, and F. Hinz, J. Phys. Met. Phys. **18**, 2033 (1988).
[17] N. Travitsky, T. Ripenbein, D. Golodnitsky, Y. Rosenberg, L. Burshtein, and E. Peled, J. Power Sources **161**, 782 (2006).
[18] A. Longo and A. Martorana, J. Appl. Crystallogr. **41**, 446 (2008).
[19] G. Agostini, R. Pellegrini, G. Leofanti, L. Bertinetti, S. Bertarione, E. Groppo, A. Zecchina, and C. Lamberti, J. Phys. Chem. C **113**, 10485 (2009).
[20] A. Di Cicco, R. Gunnella, R. Marassi, M. Minicucci, R. Natali, G. Pratesi, and S. Stizza, J. Non-Cryst. Solids **352**, 4155 (2006).
[21] J. I. Langford, D. Louër, and P. Scardi, J. Appl. Crystallogr. **33**, 964 (2000).
[22] L. Ottaviano, A. Filipponi, and A. Di Cicco, Phys. Rev. B **49**, 11749 (1994).
[23] P. Scherrer, Nachr. Ges. Wiss. Göttingen **26** (1918).
[24] J. I. Langford and A. J. C. Wilson, J. Appl. Crystallogr. **11**, 102 (1978).
[25] G. Pratesi, A. Di Cicco, M. Minicucci, and J.-P. Itiè, J. Phys. Condens. Matter **17**, 2625 (2005).
[26] A. Di Cicco, M. Minicucci, E. Principi, A. Witkowska, J. Rybicki, and R. Laskowski, J. Phys. Condens. Matter **14**, 3365 (2002).
[27] L. Vegard, Z. Phys. **5**, 17 (1921).
[28] A. R. Denton and N. W. Ashcroft, Phys. Rev. A **43**, 3161 (1991).
[29] V. S. Urusov, J. Struct. Chem. **33**, 68 (1992).
[30] *Constitution of Binary Alloys*, edited by M. Hansen (McGraw-Hill, New York, 1958).
[31] S. C. Zignani, E. Antolini, and E. R. Gonzalez, J. Power Sources **182**, 83 (2008).
[32] C. Meneghini, M. Maret, V. Parasote, M. Cadeville, J. Hazemann, R. Cortes, and S. Colonna, Eur. Phys. J. B **7**, 347 (1999).
[33] A. Di Cicco, G. Aquilanti, M. Minicucci, E. Principi, N. Novello, A. Cognigni, and L. Olivi, J. Phys. Conference Series **190**, 012043 (2009).
[34] M. O. Krause and J. H. Oliver, J. Phys. Chem. Ref. Data **8**, 329 (1979).
[35] Z. W. Lu, S.-H. Wei, and A. Zunger, Phys. Rev. B **45**, 10314 (1992).
[36] A. Filipponi and A. Di Cicco, TASK Quart. **4**, 575 (2000).
[37] E. Sevillano, H. Meuth, and J. J. Rehr, Phys. Rev. B **20**, 4908 (1979).
[38] W. Böhmer and P. Rabe, J. Phys. C **12**, 2465 (1979).